Sensitivity Study on the Influence of Cloud Microphysical Parameters on Mixed-Phase Cloud Thermodynamic Phase Partitioning in CAM5

IVY TAN AND TRUDE STORELVMO

Yale University, New Haven, Connecticut

(Manuscript received 5 June 2015, in final form 6 October 2015)

ABSTRACT

The influence of six CAM5.1 cloud microphysical parameters on the variance of phase partitioning in mixed-phase clouds is determined by application of a variance-based sensitivity analysis. The sensitivity analysis is based on a generalized linear model that assumes a polynomial relationship between the six parameters and the two-way interactions between them. The parameters, bounded such that they yield realistic cloud phase values, were selected by adopting a quasi–Monte Carlo sampling approach. The sensitivity analysis is applied globally, and to 20°-latitude-wide bands, and over the Southern Ocean at various mixed-phase cloud isotherms and reveals that the Wegener–Bergeron–Findeisen (WBF) time scale for the growth of ice crystals single-handedly accounts for the vast majority of the variance in cloud phase partitioning in mixed-phase clouds, while its interaction with the WBF time scale for the growth of snowflakes plays a secondary role. The fraction of dust aerosols active as ice nuclei in latitude bands, and the parameter related to the ice crystal fall speed and their interactions with the WBF time scale for ice are also significant. All other investigated parameters and their interactions with each other are negligible ($<3\%$). Further analysis comparing three of the quasi–Monte Carlo–sampled simulations with spaceborne lidar observations by CALIOP suggests that the WBF process in CAM5.1 is currently parameterized such that it occurs too rapidly due to failure to account for subgrid-scale variability of liquid and ice partitioning in mixed-phase clouds.

1. Introduction

An age-old problem that has existed ever since the dawn of the rise of global climate models (GCMs) is the representation of clouds on the global scale. The problem stems from the fact that processes in clouds occur at microscopic scales that cannot be resolved in GCMs; hence, these processes need to be parameterized in such models. The parameterization of these processes comes at the cost of necessitating tuning parameters that are often unphysical and lead to compensating errors (Boucher et al. 2013; McFarlane 2011).

Substantial improvements have been made to the cloud microphysical schemes implemented in the latest generation of GCMs over the years. In the case of cloud phase, there is a move afoot to eliminate fixed-temperature-ramp schemes and to instead replace them with prognostic schemes. Two-moment schemes that include both prognostic equations for number concentrations of cloud ice and droplets and mass mixing ratios have also replaced outdated one-moment schemes that only predict mass mixing ratios (e.g., Morrison and Gettelman 2008; Salzmann et al. 2010). Another notable example of an advancement in GCMs is the implementation of "statistical cloud schemes" that are based on probability distribution functions (PDFs) of cloud-related properties, such as the total water mixing ratio (e.g., Tompkins 2002), vertical velocity (e.g., Storelvmo et al. 2008; Ghan et al. 1997), and cloud fraction (e.g., Naumann et al. 2013). The statistical cloud schemes allow the representation of subgrid-scale variability in clouds properties, which reduces biases introduced by assuming homogeneous cloud properties within individual grid boxes. This, in turn, reduces the need for tuning parameters, which arises from these biases in the first place (Rotstayn 2000). Ultimately, more accurate calculations of radiative fluxes result from the representation of subgrid-scale variability (Pincus and Klein 2000).

Despite these improvements, a continuing outstanding weakness of these schemes lies in the arbitrariness of the tuning parameters there within, which

---

Corresponding author address: Ivy Tan, Geology and Geophysics, Yale University, 210 Whitney Ave., New Haven, CT 06511.
E-mail: ivy.tan@yale.edu

DOI: 10.1175/JAS-D-15-0152.1

are notoriously fraught with uncertainties. Among these parameters, few have been specifically tuned to accurately simulate thermodynamic phase partitioning in mixed-phase clouds. These clouds are ubiquitous in Earth's mid- and upper troposphere at midlatitudes and the lower troposphere in the Arctic (Shupe 2011; Hobbs and Rangno 1998; Pinto 1998; Hobbs et al. 2001; Mioche et al. 2015). They exist at temperatures between −35° and 0°C and contain a thermodynamically unstable mixture of coexisting supercooled liquid droplets and ice crystals. The contrasting optical properties and fall speeds of liquid droplets and ice crystals imply that Earth's radiative budget will delicately depend on the proportion of supercooled liquid to ice within these clouds. The latter quantity will herein be referred to as the supercooled cloud fraction (SCF) and is quantified as the fraction of supercooled liquid to the total amount of supercooled liquid and ice within a mixed-phase cloud population. In addition to the purely radiative effect of liquid droplets and ice crystals alone, various climate feedbacks act to further amplify or damp the radiative forcing effect of cloud phase. This will likely impact the transient climate response (TCR) and has been shown to result in a wide range in equilibrium climate sensitivity (ECS), which precludes accurate projections of future climate change (Mitchell et al. 1989; Li and LeTreut 1992; Tsushima et al. 2006; Choi et al. 2014). Thus, accurately representing phase partitioning in mixed-phase clouds in GCMs is critical for future climate projections. Yet less-than-desired progress has been made over the years. Comparatively scarce observations, limited understanding of the underlying microphysical mechanisms, and exorbitant computational costs are the culprits for the lack of progress seen in accurate representations of cloud phase-partitioning schemes in GCMs. A key issue recently identified in a sizable portion of atmospheric GCMs is the underestimate of SCF in mixed-phase clouds compared to satellite observations (Komurcu et al. 2014; Cesana et al. 2015). Underestimates of SCF on a global scale have been linked to underestimates in ECS (I. Tan et al. 2016, unpublished manuscript).

The current study is motivated by the uncertainties in cloud microphysical tuning parameters in GCMs and the inability of GCMs to accurately reproduce cloud phase observations that collectively lead to uncertainties in ECS and TCR. The goal is to eventually narrow the uncertainty range by systematically understanding the most important underlying mechanisms related to the microphysics of mixed-phase clouds. This is accomplished by honing in on what the authors consider to be the most relevant cloud microphysical parameters related to cloud phase in the mixed-phase cloud temperature range and subsequently searching for the combination of parameter ranges within realistic bounds that can most accurately reproduce observations of cloud phase. Thus, the goal is to eventually narrow the uncertainty ranges in ECS and TCR by accurately simulating observations of cloud phase and understanding the cloud microphysical processes responsible for controlling it, as opposed to narrowing these ranges by arbitrarily tuning parameters without physical meaning. A variance-based sensitivity analysis that is able to quantify the individual and two-way interactions between parameters is then used to assess the relative contributions of each of the parameters to the total variance in SCF. The sensitivity analysis will reveal the most relevant parameters and any of their two-way interactions with other parameters that have the greatest impact on controlling cloud phase. Insight gained from the sensitivity analysis can also be used for developing enhanced parameterizations associated with the most important processes.

The remainder of the paper is structured as follows: section 2 first describes the methodology of the current study, which takes a hybrid approach of combining model results with satellite observations; section 3 documents and offers a discussion of the results of the study, which is partitioned into two main sections, the former involving the quantification of the contribution of each of the cloud microphysical parameters to the total variance in SCF on various spatial scales and the latter analyzing strategically selected best and worst matches to satellite observations. Finally, a summary is provided, and conclusions are drawn in section 4.

2. Methodology

This section describes how global satellite observations of cloud phase were analyzed and provides a general description of the atmospheric GCM and its setup used to model satellite observations of cloud phase. Here, a description of the cloud microphysical parameters considered most relevant for tuning cloud phase to satellite observations, along with their investigated ranges, is also provided. Next, the quasi–Monte Carlo (QMC) sampling technique that was applied to obtain low-discrepancy (evenly dispersed) samples that span the full cloud microphysical parameter space is described. Details of the variance-based sensitivity analysis to quantify the relative impact of each of the cloud microphysical parameters are then given and are followed by a description of the criteria applied to judge the closest matches to satellite observations of all the QMC-sampled simulations.

a. Global CALIOP observations of supercooled cloud fractions

Global satellite observations of cloud phase were obtained by NASA's Cloud–Aerosol Lidar with Orthogonal Polarization (CALIOP) instrument. CALIOP is a dual-wavelength (532 nm, 1064 nm), 3°-off-nadir-viewing (at the present) polarization lidar (532-nm beam polarized) onboard the *Cloud–Aerosol Lidar and Infrared Pathfinder Satellite Observations* (*CALIPSO*) satellite. Launched in 28 April 2006, CALIOP flies in a sun-synchronous polar orbit with the A-train constellation at a 705-km altitude and 16-day repeat cycle that produces a footprint of 70 m along Earth's surface. Its resolution is high, taking measurements every 333 m in the horizontal and 60 m in the vertical below 8.2 km in altitude and every 60 m and 1 km in the vertical and horizontal, respectively, above 8.2 km in altitude. As the first-ever polarization lidar (polarization purity greater than 99%) to vertically measure cloud and aerosol properties throughout Earth's troposphere that made its way into orbit in space, CALIOP has been instrumental in improving the understanding of clouds and aerosol processes (Koffi et al. 2012; Cesana and Chepfer 2013).

Through its cloud–aerosol discrimination (CAD) algorithm (Liu et al. 2009), CALIOP can discriminate between clouds and aerosols in Earth's atmosphere based on statistical properties of layer volume color ratio, mean attenuated backscatter coefficient at 532 nm, depolarization, latitude, and height of the center of the layer. If a layer is identified as a cloud, it can further be classified as either a liquid or ice cloud via CALIOP's cloud phase discrimination algorithm. This algorithm discriminates between ice and liquid clouds based on the depolarization ratio, temperature, and height of the layer (Hu et al. 2009). The cloud phase discrimination algorithm heavily relies on the depolarization ratio at 532 nm, which is fundamentally based on the assumption that cloud water droplets are spherical in shape and ice crystals are irregular and nonspherical in shape. Therefore, in single-scattering events, the depolarization ratios of cloud water droplets are assumed to be zero, while those of ice crystals are assumed to be nonzero. CALIOP's cloud phase discrimination algorithm also accounts for the effects of multiple scattering, a necessary procedure given that CALIOP is a spaceborne lidar. CALIOP's cloud phase discrimination algorithm can also detect the presence of horizontally oriented ice crystals that occur as a result of weak updrafts in 30%–60% of all mixed-phase clouds, according to satellite observations (Zhou et al. 2013; Noel and Chepfer 2010; Chepfer et al. 1999). Because of the low depolarization of horizontally oriented ice crystals, the presence of these crystals can easily be confused with the presence of liquid droplets. To account for this effect, CALIOP's near-nadir-viewing geometry of 0.3° off nadir was tilted to 3° off nadir as of November 2007 to prevent specular reflection of horizontally oriented ice crystals from contaminating cloud phase discrimination and to increase the accuracy of the retrievals of extinction profiles in ice clouds (Hu et al. 2009). If the layer is instead identified as one consisting of aerosols based on the aforementioned statistical properties, then it is classified into one of six aerosol categories (dust, polluted dust, smoke, clean continental, polluted continental, and clean marine) (Omar et al. 2009).

CALIOP CALCULATIONS OF SUPERCOOLED CLOUD FRACTIONS

The current study focuses on observations of cloud phase, quantified by SCF, at the mixed-phase cloud-top temperatures of −10°, −20°, and −30°C. The isotherms were obtained using National Centers for Environmental Prediction–Department of Energy (NCEP–DOE) Reanalysis-2 data of air temperature and geopotential height at a resolution of 2.5° longitude by ~2.5° latitude (Kanamitsu et al. 2002). Versions 3.01–3.03 of CALIOP's level 2 vertical feature mask, which include observations spanning from November 2007 to June 2014 were used to compute SCFs, here defined as SCF = $\mathrm{SCF} = f_{\mathrm{liquid}}/(f_{\mathrm{liquid}} + f_{\mathrm{ice}})$, where f_{liquid} and f_{ice} are the number of footprints classified as liquid and ice clouds, respectively. Footprints classified as ice clouds are composed of both randomly and horizontally oriented ice crystals. Note that CALIOP does not have a mixed-phase cloud category. Several precautions were taken in analyzing the data. To avoid misclassifications by the CAD algorithm, data with low-confidence CAD scores were filtered out, and only data with medium- and high-confidence CAD scores were analyzed. In addition, since solar background noise degrades the signal-to-noise ratio of the 532-nm channel, daytime data were excluded from the analysis. Note that, although CALIOP is able to measure the vertical distribution of clouds and aerosols, its beam extinguishes when it passes through any medium with an optical depth $\tau > 3$. More details on the methodology of calculating SCFs from CALIOP observations can be found in Choi et al. (2010) and Tan et al. (2014).

b. CAM5.1-modeled supercooled cloud fractions

The National Center for Atmospheric Research (NCAR)'s widely used standalone atmospheric GCM, the Community Atmosphere Model, version 5.1

(CAM5.1), was used as the model of choice for this study. CAM5.1 is a freely available model that contains a state-of-the-art two-moment cloud microphysics scheme that computes number and mass concentrations of cloud condensate and ice as prognostic variables (Morrison and Gettelman 2008). This model can be run in conjunction with land, sea ice, and ocean components as part of a complete Earth system model [the Community Earth System Model (CESM)], making it particularly desirable for the purposes of the current study and its companion study to follow (I. Tan et al. 2016, unpublished manuscript). For a general description of CAM5.1, the reader is referred to Neale et al. (2010).

1) CAM5.1 SETUP

For the purpose of the current study, CAM5.1 was run at a horizontal resolution of ~4° latitude by 5° longitude and vertical resolution of 30 levels. The highest level of the model reaches ~2 hPa, which corresponds to ~40 km in height. These levels are spaced approximately 1200 m apart in the free troposphere and lower stratosphere. The resolution, although relatively coarse, is sufficient for the topics of interest in this study. Additional CAM5.1 simulations run at ~1.9° latitude by 2.5° longitude confirmed that no appreciable differences in SCF between the two horizontal resolutions exist (not shown). Three months were allocated for spinup, and SCF calculations are based on 12-month averages after the spinup period. The three-mode Modal Aerosol Module (MAM3), which includes representations of lognormal size distributions of aerosols grouped into the Aitken, accumulation, and coarse modes, was used in this study (Liu et al. 2012). All simulations were run with the finite-volume dynamical core and a model time step of 30 min.

Before running any of the simulations, the aforementioned issue of excessively low SCFs found in atmospheric GCMs in comparison with satellite observations, to which CAM5.1 is no exception, must first be addressed. The low SCFs simulated in the out-of-the-box control CAM5.1 are too low to the point that the model is not capable of simulating observations of cloud phase in the actual atmosphere. In out-of-the-box CAM5.1, SCFs are particularly unrealistically low, generally underestimating CALIOP-observed SCFs by over 90% in some regions. Upon investigation, the out-of-the-box CAM5.1 convective detrainment scheme was found to be among the causes contributing to the underestimate of SCFs in mixed-phase clouds. In the out-of-the-box detrainment scheme, cloud condensate detrained from the convective parameterization is separated into three regimes within the mixed-phase cloud temperature range (Morrison and Gettelman 2008). At temperatures warmer than −10°C (regime I), the ratio of ice to total cloud condensate detrained from convective air masses F_{det} vanishes. Between −40° and −10°C (regime II), F_{det} is a linear function of temperature. At temperatures below −40°C (regime III), $F_{\mathrm{det}} = 1$. This detrainment scheme, which led to much lower SCFs than those observed, was modified such that the temperature threshold of −10°C in the out-of-the-box scheme was replaced by −30°C (Fig. 1). The convective detrainment scheme was chosen as the means to increase SCFs to be within the range of observations for two reasons. First, doing so does not interfere with cloud microphysical parameters, some of which are tuned in this study. Second, the convective detrainment scheme is based on a temperature ramp, which is a practice that is gradually being abandoned in GCMs (e.g., Song and Zhang 2011).

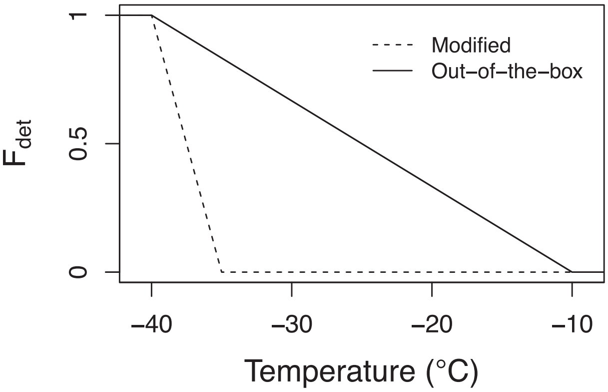

FIG. 1. The ratio of ice to total cloud condensate detrained from convection F_{det} for the out-of-the-box CAM5.1 (Morrison and Gettelman 2008) and after modification to increase SCFs in this study. SCFs simulated using the original convective detrainment scheme underestimated those from CALIOP observations by 20%–30% worldwide.

In addition to modifying the detrainment scheme to increase SCFs, the default Meyers et al. (1992) immersion and deposition ice nucleation scheme present in the out-of-the-box CAM5.1 has been replaced with an updated ice nucleation scheme by DeMott et al. (2015). This updated scheme is based on field observations [Eq. (A13)] and diagnoses ice nuclei (IN) concentrations as a function of the concentration of large dust particles. The DeMott et al. (2015) ice nucleation scheme is preferred over the Meyers et al. (1992) scheme for two main reasons. First, it computes the ice nucleating particle number concentration based on prognostically calculated aerosol number concentrations instead of assuming a fixed dependence on temperature and supersaturation that fails to take spatial and temporal variability into account. Second, it is based on surface

TABLE 1. Description of the six selected CAM5.1 cloud microphysical parameters modified in the 256 simulations selected via QMC sampling, along with their investigated ranges.

Process investigated	Relevant parameter	Default value	Investigated range
Fraction of dust aerosols active as IN	fin	1	[0, 0.5]
WBF time-scale exponent for ice	epsi	0	[−6, 0]
WBF time-scale exponent for snow	epss	0	[−6, 0]
Fraction of aerosols scavenged in stratiform clouds	sol_facti	1	[0.5, 1]
Fraction of aerosols scavenged in convective clouds	sol_factic	0.4	[0.2, 0.8]
Related to the ice crystal fall speed (s^{-1})	ai	700	[350, 1400]

level and aircraft in situ observations obtained over a wide range of seasons and regions. CAM5.1 with the DeMott et al. (2015) ice nucleation scheme and the change in the convective detrainment scheme will serve as the new ‘‘default’’ (as opposed to the out-of-the-box) model to which adjustments of the cloud microphysical parameters changes will be made. Note that the out-of-the-box Bigg immersion scheme (Bigg 1953) was deactivated, while the Young contact-freezing scheme (Young 1974), as well as the Cotton parameterization (Cotton et al. 1986) of the Hallet–Mossop process were activated and not modified in this study.

2) CAM5.1 CLOUD MICROPHYSICAL PARAMETERS

Of the many parameters associated with microphysical processes that influence cloud phase, six deemed by the authors to be most important for phase partitioning were selected as tuning parameters. The parameters (Table 1) are (i) the fraction of dust particles active as IN (fin), (ii) the Wegener–Bergeron–Findeisen (WBF) process time scale that determines the growth of ice crystals at the expense of liquid droplets (a corollary that follows from the lower saturation vapor pressure of ice relative to liquid water) (epsi), (iii) the WBF process time scale for snowflakes (epss), (iv) one related to the ice crystal fall speed (ai), and wet scavenging of aerosols in (v) stratiform (sol_facti) and (vi) convective clouds (sol_factic). The primary driving equations in which these parameters appear are given in the appendix.

The parameter fin in this study is the fraction that is multiplied by the concentration of IN that nucleate ice via condensation, immersion, and deposition freezing in the DeMott et al. (2015) scheme. The investigated range for fin is limited to half of that in the original parameterization for two main reasons: first, certain minerals in dust aerosols are more efficient at ice nucleation than others (Atkinson et al. 2013), implying that not all dust aerosols in the atmosphere are active as IN; and second, because CAM5.1, among other atmospheric GCMs, severely underestimates SCFs in mixed-phase clouds (Komurcu et al. 2014; Cesana et al. 2015), potentially because IN are overestimated in GCM parameterizations.

The WBF process is possibly the most inaccurately parameterized of all the investigated processes in this study. Accurately representing the WBF process is motivated by the central role it plays in mixed-phase cloud formation. The main limiting factor in accurately modeling the WBF process is the lack of representation of the subgrid-scale variability in cloud liquid and ice within mixed-phase clouds (Storelvmo et al. 2008). Most atmospheric GCMs define a threshold cloud mixing ratio above which the entire grid box glaciates, when, in fact, observational evidence obtained from field campaigns and satellite measurements suggest against this assumption. Rather, ice crystals and liquid droplets are usually found clustered in pockets horizontally spanning anywhere from the order of 10 m, for example, in the Arctic (Chylek and Borel 2004) to a few kilometers in mid- and high latitudes (Korolev et al. 2003; Field et al. 2004). While no such threshold mixing ratio exists in CAM5, unrealistic maximum overlap in ice crystals and liquid droplets within mixed-phase clouds do exist in CAM5, implying that liquid is maximally depleted in the process of ice depositional growth rate in the WBF process. Furthermore, the subgrid-scale variability involved in the WBF process in CAM5 is inaccurately taken into account by assuming a gamma distribution with fixed variance for liquid water content (Fan et al. 2011). In other words, the fact that, on subgrid scales, pockets of ice and liquid are actually observed in the atmosphere instead of artificial homogeneous mixtures of ice and liquid implies that there is often an overestimate in the efficiency of the WBF time scale lurking in atmospheric GCMs. In the most extreme case, this assumption results in a six-order-of-magnitude overestimate in volume where the WBF process occurs compared to actual observations that suggest that uniform mixing occurs on scales as small as tens of meters (Fig. 2). This difference in volume translates to a difference of up to six orders of magnitude in the time scale of the WBF process since the local in-cloud deposition rate of water vapor onto cloud ice is assumed to scale

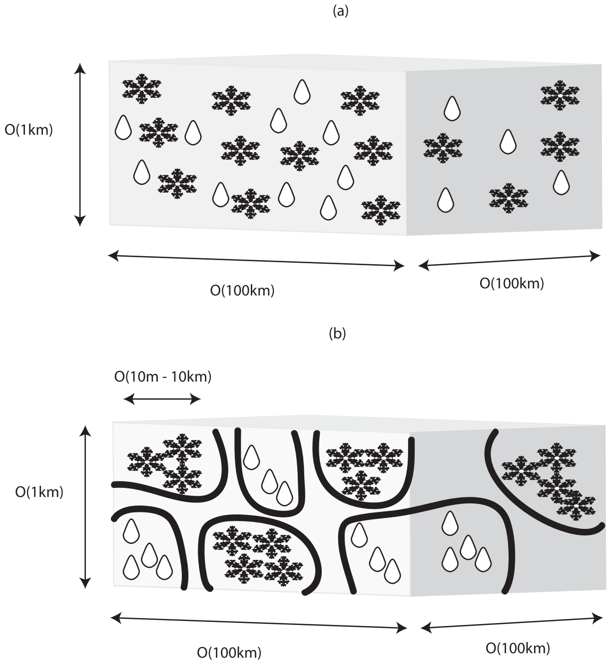

FIG. 2. Schematic diagrams contrasting (a) the idealized homogeneous mixture of ice/snow and liquid within a GCM grid box, which typically spans on the order of 100 km in the horizontal and 1 km in the vertical, with (b) the more realistic heterogeneous mixture of ice/snow and liquid that usually exists in separate pockets of liquid and ice on the order of tens of meters to 20 km according to satellite and field observations. The gray-shaded regions represent the mixing zones, where liquid droplets and ice crystals interact via the WBF process. In (a), the entire grid box is the mixing zone. In (b), the mixing zone is reduced to include only the regions outside the outlined pockets.

linearly with the WBF time scale (see the appendix, section a). Hence, in the current study, epsi and epss, the parameters that control the time scale of the WBF process for ice and snow, respectively, unlike the other parameters investigated in this study, are actually exponents ranging from −6 to 0 to reflect observed subgrid-scale variability. It is also noteworthy that test simulations with CAM5.1 have revealed that the effect of the WBF time scale on zonally averaged SCF saturates when the process is retarded by six orders of magnitude (not shown). The WBF time scale is most greatly affected by mixing processes in the atmosphere, which homogenize ice crystals and liquid droplets in mixed-phase clouds. Regions distantly separated from regions of convection and the atmospheric boundary layer are therefore expected to exhibit more subgrid-scale variability. Although most of the uncertainty in the WBF time scale is associated with subgrid-scale variability, minor contributions are attributed to uncertainties in the spectral parameters related to the size distribution of ice crystals and the diffusivity of water vapor [see Eqs. (A3) and (A6)].

The ranges of the other three parameters, which are the ice crystal fall speed–related parameter and the fraction of aerosols scavenged in stratiform and convective clouds, were selected following Zhao et al. (2013), who performed sensitivity analyses on the effects of 16 cloud and aerosol parameters within realistic ranges. Their sensitivity analyses determined how the individual and two-way interactions between the parameters influenced the variance in top-of-the-atmosphere (TOA) radiative fluxes, a quantity that is closely linked to SCFs. These three parameters were selected on the basis that they were found to be the next most influential processes in the variance in radiative flux in CAM5.1 according to Zhao et al. (2013). All parameter ranges used in this study are summarized in Table 1.

3) CAM5.1 CALCULATIONS OF SUPERCOOLED CLOUD FRACTIONS

Following Komurcu et al. (2014), SCFs modeled by CAM5.1 are calculated at the $-10^\circ \pm 1^\circ\mathrm{C}$, $-20^\circ \pm 1^\circ\mathrm{C}$, and $-30^\circ \pm 1^\circ\mathrm{C}$ isotherms as $\mathrm{SCF} = r_{\mathrm{liquid}}/(r_{\mathrm{liquid}} + r_{\mathrm{ice}})$, where r is the mixing ratio. To allow for fair comparisons between the modeled SCFs with CALIOP observations of SCF, only mixing ratios at cloud tops were included in the calculations, except in the case of optically thin clouds ($\tau < 3$), where mixing ratios in lower cloud layers are also included. Although SCFs calculated from CALIOP observations are based on footprints that essentially determine the frequency of occurrence of liquid and ice cloud layers, the much higher resolution of the observations renders them comparable to those modeled by CAM5.1.

c. Quasi–Monte Carlo sampling of the cloud microphysical parameter space

The two goals of this study were borne in mind when selecting combinations of the cloud microphysical parameters listed in the previous section. The first goal is to simulate satellite observations of cloud phase as accurately as possible by probing the six-dimensional space of parameters within their realistic ranges. The second goal is to determine the most influential parameters on cloud phase. QMC sampling through the use of a Halton sequence is advantageous for this purpose since it can span the full parameter space while deterministically minimizing the discrepancy between sample points, thereby guaranteeing good dispersion between them (Caflisch 1998). By probing the full parameter space, QMC sampling fulfills the two aforementioned goals by effectively checking a large number of combinations that may reproduce satellite observations, while simultaneously providing a sample set that spans the full parameter space necessary for a sensitivity analysis. When considering the total number of simulations to perform, the trade-off between computational cost and numerical error must be considered, and thus a total of 256 combinations of the six parameters were obtained using the QMC sampling method as in Zhao et al. (2013).

d. Sensitivity analysis

This study employs the method of Zhao et al. (2013), who applied a generalized linear model (GLM) after completion of the 256 QMC-sampled simulations to carry out a variance-based sensitivity analysis. The GLM assumes a polynomial relationship between the cloud microphysical parameters and CAM5.1-modeled SCF and determines whether perturbations to the parameters through their individual and two-way interactions with each other significantly influence variance in SCF through null hypothesis testing. Note that the polynomial assumption is inappropriate if the fitted variance is too small (i.e., $R^2 \sim 0$) (Zhao et al. 2013). The GLM can then rank, as a percentage, the contributions of the statistically significant individual and two-way interactions between the input parameters to the total variance in SCF. The GLM can be written as

$$Y^i = \beta_0 + \sum_{j=1}^{n} \beta_j p_i^j + \sum_{j=1}^{n} \sum_{k=1}^{n} \beta_{j,k} p_j^i p_k^i + \varepsilon_i, \quad \varepsilon_i \overset{\text{iid}}{\sim} N(0, \sigma^2), \tag{1}$$

where Y^i is the ith response variable, SCF; β_j and $\beta_{j,k}$ are coefficients of the linear (individual) and two-way interaction terms, respectively; and p_i^j (p_i^k) are the ith realization of the jth (kth) parameter. The index i runs from 1 to 256, and $n = 6$. The residual of the ith realization is given by ε_i. The residuals are assumed to follow a zero-mean, unit-variance normal distribution. The null hypothesis assumes that the regression coefficients $\widehat{\beta_i}$ are zero, and the t statistic for the null hypothesis is given by $t = \widehat{\beta_i}/\mathrm{SE}(\widehat{\beta_i})$. Parameters are deemed significant when the corresponding $P < 0.05$. In this study, the GLM is applied on the global scale, to 20°-latitudinal-wide bands, and separately over the Southern Ocean.

There are two main advantages of using the QMC/GLM approach for sensitivity analysis. First, unlike one-at-a-time sensitivity analyses that operate by varying only one parameter at a time while holding all other parameters constant, the GLM is able to take interaction effects between parameters into account (Zhao et al. 2013). Second, QMC sampling of the parameter space for the GLM sensitivity analysis is an efficient way of sampling a full multidimensional parameter space that cannot be achieved with one-at-a-time sensitivity analyses.

e. Selection criteria

To quantitatively determine the simulations that best match CALIOP observations of cloud phase, the SCF score is defined as

$$\text{SCF score}(i,j) = \overline{\mathrm{SCFM}_{i,j}} - \overline{\mathrm{SCFO}_{i,j}}, \tag{2}$$

where $\mathrm{SCFM}_{i,j}$ is the average CAM5.1-modeled SCF, and $\mathrm{SCFO}_{i,j}$ is the average CALIOP-observed SCF at the ith 20°-latitude-wide bands and jth isotherm (either −10°, −20°, or −30°C). The overline denotes a time average (the last year of simulation for CAM5.1 and the full 79-month period for CALIOP observations). In assessing which simulations perform best overall among all nine latitude bands and all three isotherms, the cumulative SCF score (CS score) is introduced as

$$\text{CS score} = \sum_{j=1}^{n} \sum_{i=1}^{m} (\overline{\mathrm{SCFM}_{i,j}} - \overline{\mathrm{SCFO}_{i,j}}). \tag{3}$$

In selecting the simulations that most accurately reproduce CALIOP observations, the goal is to select the simulations with the lowest CS scores, that is, those with the smallest overall differences between modeled and observed SCFs in all three dimensions at grid boxes resolved at 4° latitude by 5° longitude, averaged over 20°-latitude-wide bands and at the three select isotherms of −10°, −20°, and −30°C. Note that, according to this convention, lower-scoring simulations are synonymous with better-scoring simulations.

3. Results and discussion

In what follows, the results of the GLM sensitivity analyses are first reported. The QMC-sampled simulations that best meet the selection criteria for matching CALIOP observations are then analyzed and discussed. Finally, focus is given to the most influential parameter according to the GLM sensitivity analyses and how its range impacts the ability to reproduce CALIOP observations in latitude bands. This is followed by physical interpretation of the results. The validity of the underlying polynomial assumption in the GLM is justified in each application.

a. Sensitivity of supercooled cloud fraction to the cloud microphysical parameters

The results of the GLM sensitivity analyses are partitioned into three sections, each describing the analysis in different regions. The results on the global

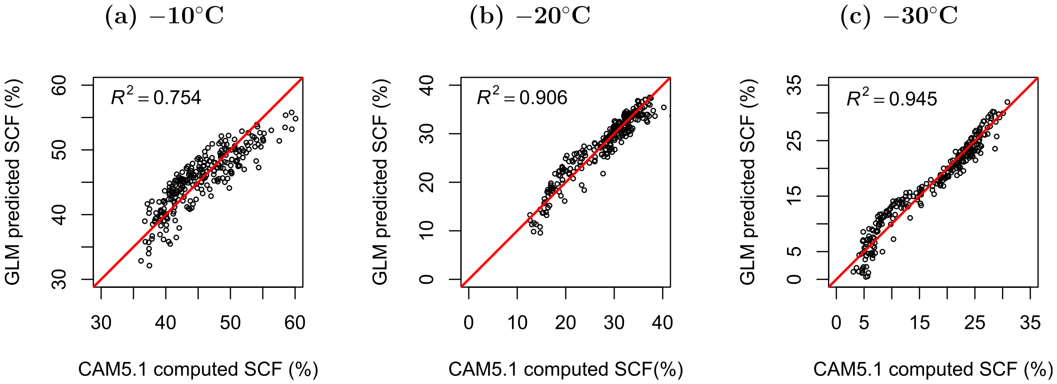

FIG. 3. Globally averaged GLM-predicted SCFs as functions of globally averaged CAM5.1-modeled SCFs at the (a) −10°, (b) −20°, and (c) −30°C isotherms. The GLM is able to explain 75.4%, 90.6%, and 94.5% of the variance in CAM5.1-modeled SCFs at the respective isotherms on the global scale. The plots substantiate the validity of the polynomial assumption in the GLM.

scale are first discussed and analyzed, and these are followed by results in 20°-latitude-wide zonal bands. Special focus is given to the Southern Ocean in the last section.

1) ON THE GLOBAL SCALE

To be able to apply the GLM for sensitivity analysis, the assumption that the polynomial relationship in Eq. (1) is reasonable must first be established. A plot of the globally averaged GLM-predicted SCFs as a function of the globally averaged CAM5.1-modeled SCF confirms that the polynomial assumption is indeed valid on the global scale at the three mixed-phase cloud isotherms; the R^2 values of 0.754, 0.906, and 0.945 indicate that the GLM explains 75.4%, 90.6% and 94.5% of the variance in CAM5.1-modeled SCF at the −10°, −20°, and −30°C isotherms, respectively (Fig. 3). It is important to note the relatively low R^2 value at the −10°C isotherm; results at this particular isotherm should therefore be interpreted with caution. Highly nonlinear interactions between the variables and multiple-way interaction effects account for deviations from the polynomial assumption, and, hence, low R^2 values.

With the basis of the GLM applied on the global scale now established, the results can be conveniently visualized at a glance in the form of heat maps (Fig. 4). These heat maps show the relative contribution of the main (on the diagonal) and interaction (on the off diagonal) effects of the six parameters to the total variance in globally averaged SCF across three mixed-phase cloud isotherms. What is immediately apparent from these heat maps is that the vast majority of parameters and their interactions with each other contribute very little (<10%) to the total variance in globally averaged SCF at each of the individual three isotherms. In fact, at approximately midway into the mixed-phase cloud temperature range of −20°C, aside from the contribution of ~15% to the total variance in SCF that derives from the interaction between epsi and epss (the two parameters associated with the rate at which ice and snow, respectively, grow at the expense of liquid droplets in the WBF process), the individual effect of epsi accounts for 66% of the total variance in globally averaged SCF. At the −30°C isotherm, the individual effect of epsi is even more pronounced; it alone accounts for ~85% of the total variance in SCF on the global scale. In contrast, the relative contribution of the interaction effect between epsi and epss of ~39% outweighs the individual effect of epsi of ~15% at the −10°C isotherm. These results are logical, as ice crystals become present in larger quantities and snowflakes diminish in quantity as homogeneous freezing temperatures are approached, therefore causing the WBF process associated with snowflakes (ice) to exert a relatively stronger influence at warmer (colder) mixed-phase cloud temperatures. Note that the default threshold size for the autoconversion from ice to snow is 400 μm. Self-collection processes for ice and snow are parameterized; however, the collection of droplets by cloud ice is neglected in CAM5.1.

The parameters with the next most significant contributions to the total variance in globally averaged SCFs are fin and ai. On the global scale, the contribution of fin is largest at the −10°C isotherm (~21%) and diminishes with decreasing temperature, accounting for ~12.8% and ~5.9% of the total variance in SCF at the −20° and −30°C isotherms, respectively. This result is expected, as IN are the primary means by which ice crystals are found at mixed-phase cloud temperatures, holding true to a greater extent at temperatures further from the homogeneous freezing temperature. Ice crystal

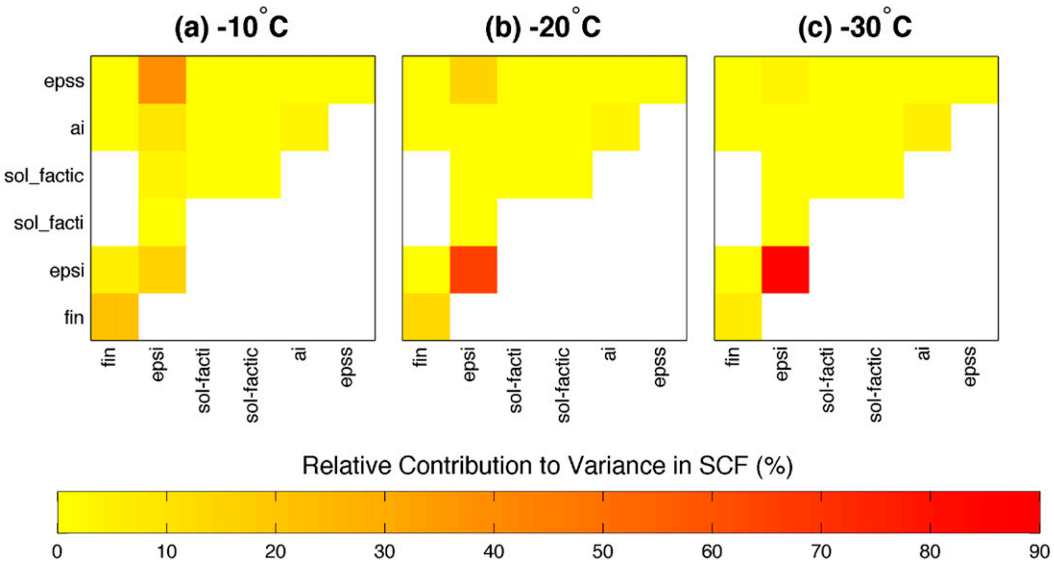

FIG. 4. Heat maps of the relative contribution of main (displayed on the diagonal) and interaction effects of the six cloud microphysical parameters to the total variance globally averaged SCF, based on the GLM sensitivity analysis of the QMC-sampled simulations at the (a) −10°, (b) −20°, and (c) −30°C isotherms. The white space indicates statistically insignificant ($P < 0.05$) or redundant values.

fall speed, on the other hand, in theory, should be expected to be more important at colder mixed-phase cloud temperatures, since ice crystals are expected to be more ubiquitous at colder temperatures in Earth's atmosphere. Indeed, ai contributes more to the total variance in globally averaged SCF at the −30°C isotherm (~5.0%) than at the other two isotherms; it does, however, contribute less at the −20°C isotherm than at the −10°C isotherm (~4.1% vs ~3.2%). The latter unexpected effect may be attributed to the overestimate of IN at temperatures warmer than −12°C typically assumed in climate models (Conen et al. 2015).

On the global scale, the interaction between fin, sol_factic and sol_facti, and the individual effect of sol_facti are statistically insignificant ($P > 0.05$) at all three isotherms (as indicated by the blank spaces). All other interactions are statistically significant. Note that the statistical significance of these values will depend on the range of the parameters as well. Note also that, although some of these simulations may result in off-balance top-of-the-atmosphere radiation budgets, they can be tuned if coupled to a responding climate system. Since these simulations were run with fixed sea surface temperatures, further tuning beyond what is described in the manuscript is not applicable.

2) IN ZONAL BANDS

In the previous section, the GLM revealed which parameters and their interaction effects are generally most important at the three isotherms on the global scale; however, SCF greatly varies on the global scale, as evidenced by satellite observations (Tan et al. 2014), therefore warranting further analyses on a more localized scale. The GLM sensitivity analysis was therefore then applied to 20°-latitude-wide bands at the same three isotherms to break down the contributions of the parameters and their interactions into latitude bands (Fig. 5). When applied to the nine 20°-latitude-wide bands at each isotherm, the GLM sensitivity analysis generally explains 80%–90% of the variance in CAM5.1-modeled SCF, and, at the very least, in a few rare cases which will be pointed out, 54.1%, 71.4%, and 68.1% of the variance in CAM5.1-modeled SCF at the −10°, −20°, and −30°C isotherms, respectively. The polynomial assumption is therefore valid for all regions examined in this study; however, the authors reiterate that regions with low R^2 values should be interpreted with caution.

The most prominent feature common to all three isotherms is the dominating effect of epsi, as expected from the heat maps in Fig. 4. The parameter epsi singlehandedly accounts for most of the variance in SCF at all latitude bands, except at those between 30°S and 30°N at the two colder isotherms (Figs. 5b and 5c). The 10°S–10°N band at the −20° and −30°C isotherms should be interpreted with caution because of the relatively low R^2 values of 0.71 and 0.68, respectively. From the global analysis shown by the heat maps in Fig. 4, the interaction between epsi and epss and the individual

(a) −10 °C

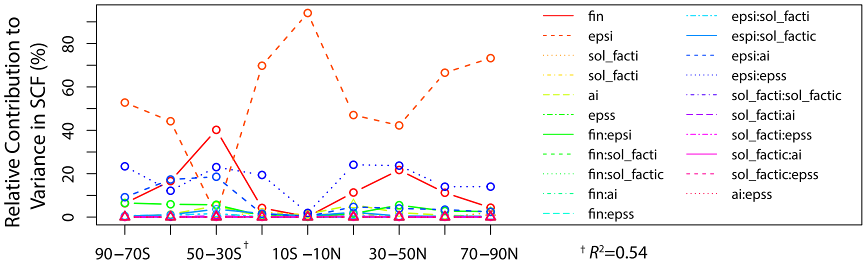

(b) −20 °C

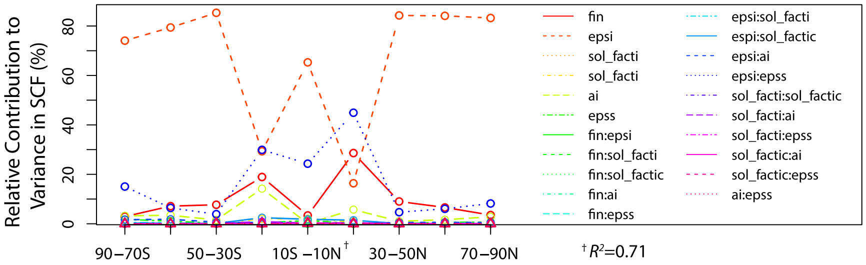

(c) −30 °C

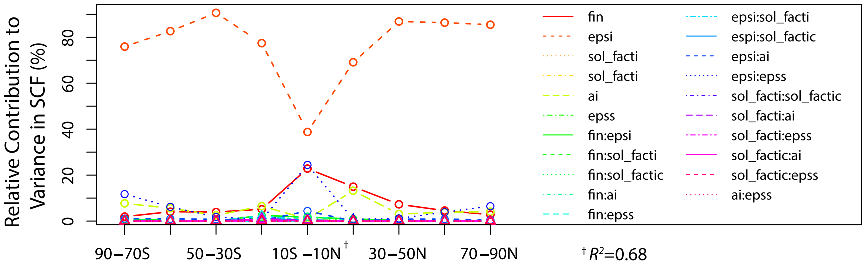

FIG. 5. Relative contribution of individual parameters and two-way interactions (denoted by the colons) between them to the variance in SCF in 20°-latitude-wide bands at the (a) −10°, (b) −20°, and (c) −30°C isotherms based on the GLM sensitivity analysis. Statistically significant [i.e., $P < 0.05$ (insignificant, i.e., $P > 0.05$)] data points are represented by circular (triangular) points. The reader is advised to interpret the marked bands with caution because of the low R^2 values.

effect of fin are significant at the −10° (Fig. 4a) and −20°C isotherms (Fig. 4b). A comparison with Fig. 5 shows that these effects are only important outside the tropics. The effect of fin naturally derives from the latitude bands containing the Taklimakan and Sahara Deserts (Figs. 5a and 5b, respectively). The sensitivity to ice nucleation by dust aerosols in these regions (related to fin) presumably increases ice crystal formation in mixed-phase clouds, where there would otherwise be more liquid droplets, thereby actively involving the WBF process time scale for snowflakes (related to epss) and ice crystal sedimentation speed on influencing SCF (related to ai in Figs. 5b and 5c). These processes appear to be intertwined at the −20° and −30°C isotherms.

At the −10°C isotherm, the relative contributions of epsi to the variance in globally averaged SCFs seen in Fig. 4 underestimate those seen in the zonal averages. The polynomial relationship used in the GLM, however, is generally a better assumption for the zonal averages (mean $R^2 = 0.845$ across the nine latitude bands in Fig. 5a) than the global averages ($R^2 = 0.754$ for Fig. 4a) at this isotherm, except at the 30°–50°S band ($R^2 = 0.541$ in Fig. 5a), and therefore lends more credibility than the results on the global scale. It is therefore more likely that epsi also plays a more critical role at the −10°C isotherm than shown by the global analysis. Although not quantitatively as reliable, the analysis on the global scale, however, still points out the key important parameters and their interactions that are

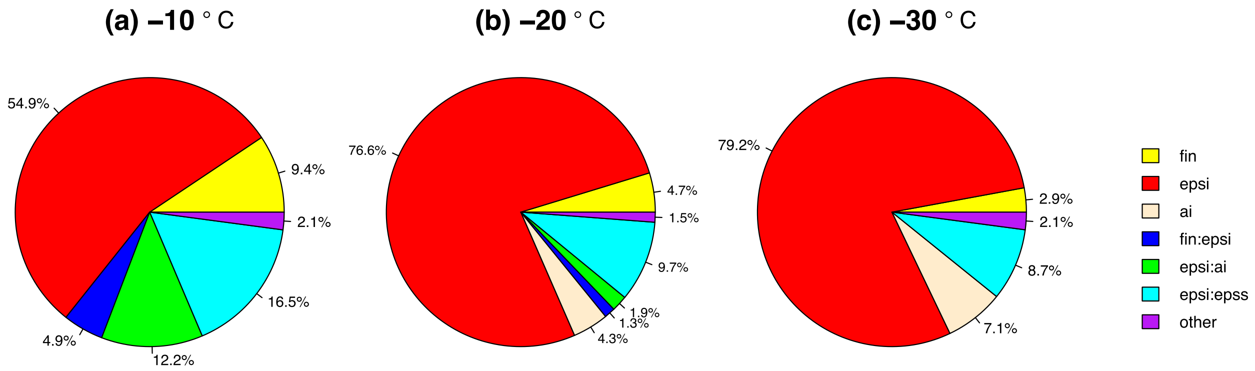

FIG. 6. Relative contribution of key individual parameters and two-way interactions (denoted by colons) between them to the variance in SCF over the Southern Ocean, spanning the region from 58° to 90°S at the (a) −10°C ($R^2 = 0.893$), (b) −20°C ($R^2 = 0.953$), and (c) −30°C ($R^2 = 0.969$) isotherms based on GLM sensitivity analysis. These R^2 values quantify the ability of the GLM polynomial assumption to explain the variance in CAM5.1-simulated SCFs. All contributions excluding those in the ''other'' category are statistically significant (i.e., $P < 0.05$).

most important for determining SCF variance. Unlike the two colder isotherms, the interaction between fin and epsi shown in Fig. 5a plays a more important role in influencing the variance of SCF, in agreement with Tan et al. (2014), who found stronger negative correlations between dust aerosols and SCF at the −10°C isotherm than at other mixed-phase cloud isotherms based on CALIOP observations. As with the two colder isotherms (Figs. 5b,c), the interaction between epsi and epss continues to play a significant role at the −10°C isotherm as well (Figs. 5a).

In comparison to Zhao et al. (2013), two-way interactions effects were also found to be negligible in this study relative to the individual effects of a few key parameters. However, whereas Zhao et al. (2013) found that the size threshold for the autoconversion from ice to snow (dcs) dominated variance in radiative fluxes at the TOA, the current study finds that epsi is the parameter that dominates SCF variance. Although Zhao et al. (2013) found dcs to be by far the most influential parameter in controlling variance in TOA radiative fluxes, the parameter was purposely excluded from this study since snow is not included in the SCF calculation of this study. Snow is intentionally excluded in the SCF calculations of the current study since the CALIOP calculations of SCF, which the CAM5.1 simulations strive to reproduce, do not include snow. The CALIOP lidar is unable to penetrate far into clouds (its detection limit is $\tau \sim 3$), so this study only takes measurements at cloud tops into account, where snow is unlikely to be present. Accounting for snow in the SCF calculations would therefore always lead to an underestimate of SCF compared to CALIOP observations. Since CALIOP is unable to detect snow in mixed-phase clouds, dcs was thus excluded as a parameter in this study to allow for fair comparisons with CALIOP observations of SCFs. It is also worth noting that autoconversion is not a real physical process that occurs in the actual atmosphere and is instead purely used as a tuning parameter. For this reason, there is a need to eventually eliminate dcs in future improved models (Eidhammer et al. 2014).

3) OVER THE SOUTHERN OCEAN

As a cloudy region with substantial low cloud cover associated with high uncertainties in cloud albedo responses to a warmed climate (Zelinka et al. 2012; McCoy et al. 2014), the Southern Ocean is a region of particular interest. A GLM sensitivity analysis was performed for the region extending from 58° to 90°S, covering the entire expanse of the Southern Ocean at mixed-phase cloud temperatures (Fig. 6). In the Southern Ocean, the same parameters and their interactions with each other more or less affect the three isotherms; however, the extent to which they contribute to SCF variance differs considerably. The parameter epsi continues to dominate the variance in SCF at all isotherms, followed by its relatively weaker but nevertheless important interaction with epss, but the lone effect of ai only becomes appreciable at the two colder isotherms. As a particularly pristine region, the Southern Ocean is relatively free of aerosols. Thus, at colder isotherms, the effect of fin is relatively small, contributing to at least half of what it does at the −10°C isotherm. This presumably occurs because IN, if present in this pristine region, do not get lofted to high altitudes. The influence of ai therefore potentially at least partially derives from homogeneously nucleated ice from cirrus clouds aloft.

At the −10°C isotherm, the contribution of epsi is downplayed by fin and interactions between epsi and each of the three parameters epss, ai, and fin. Any trace amounts of IN found in the IN-scarce region of the

TABLE 2. Cloud microphysical parameter values rounded to the hundredth decimal place for the best- and worst-scoring simulations and the two selected best-scoring simulations with contrasting parameter ranges, along with their CS scores.

Simulation	fin	epsi and epss	sol_facti	sol_factic	ai (s^{-1})	CS score
CALIOP-169	0.024	−1.23	0.72	0.74	690.78	140.09
CALIOP-7	0.19	−0.096	0.99	0.97	371.085	186.72
CALIOP-172	0.49	−1.62	0.96	0.72	354.28	220.75
CALIOP-50	0.37	−5.35	0.87	0.58	711.24	442.97
CAM5.1 default	1	0	1	0.4	700	492.45
CAM5.1 out of the box	— (Meyers et al. 1992)	0	1	0.4	700	512.49

Southern Ocean are expected to decrease SCFs more than they would in another region ubiquitous in IN. IN lofted to low altitudes in this region appear to contribute to quite a significant portion of the variance in SCF (just under 10%), although not nearly as much as it does over the desert regions discussed above. A particular feature that stands out in the Southern Ocean, however, is the ~5% contribution of the interaction between fin and epsi found only here and in desert regions at the −10°C isotherm. This feature demonstrates the sensitivity of the Southern Ocean to any trace amount of IN found in the region. Aside from the individual effect of epsi, the subsequent ice crystal fall speed (associated with ai) after its formation by way of the WBF process and the interaction between the WBF processes for ice and snow are the two next largest contributors to SCF variance in the Southern Ocean.

b. *Selected simulations and their comparisons with CALIOP observations*

The second objective of this study is to select a handful of the QMC-sampled CAM5.1 simulations with low CS scores, a diagnostic that was defined to identify which simulations are the most well rounded in reproducing CALIOP observations of SCF in three-dimensional space (discretized into 4°-latitude-by-5°-longitude grid boxes and at the −10°, −20°, and −30°C isotherms).

As a starting point, the simulation with the lowest CS score, which will be referred to by its technical name, CALIOP-169, was selected. Note that, since the CS scores were calculated over 20°-latitudinal-wide bands, certain combinations of parameter values frequently result in simulations that score very well in one particular band or isotherm but also very poorly in another band or isotherm. The CS score combines these cancellation effects and simply scores simulations based on how well rounded they are overall. Instead of exclusively utilizing CS scores to stringently select the other best matches, selecting a group of simulations that span a wide parameter range, especially in epsi, epss, and fin, the three most influential parameters as determined by the GLM sensitivity analysis then became the most important criterion so long as the CS score is within a reasonable range of CALIOP-169, which has a CS score of 140.09. To this end, two more simulations, CALIOP-7 and CALIOP-172, with CS scores of 186.72 and 220.75, respectively, were selected. These CS scores should be compared to that of the simulation with the highest CS score, CALIOP-50, which has a value of 442.97, and those of the default CAM5.1 and out-of-the-box CAM5.1 simulations (492.45 and 512.49, respectively). Table 2 compares the CS scores of the three selected simulations with each other and with the simulation with the highest CS score; parameter values are listed alongside.

The global distributions of SCFs at the three isotherms as observed by CALIOP, differenced with the three selected simulations, the simulations with the highest CS score, and as modeled by the out-of-the-box CAM5.1 model are shown in Fig. 7. The most striking feature of Fig. 7 is the severe underestimate of SCFs, especially in the extratropics of the two warmer isotherms in the out-of-the-box CAM5.1 and default CAM5.1 shown in the bottom panel. Note that the coldest isotherm performs relatively well in comparison to the other two isotherms in these two simulations. Although this is not a region where strong mixing processes occur, there is not much supercooled liquid to begin with, since the temperature is close to the homogeneous freezing temperature. The pattern root-mean-squared errors (RMSEs), correlation coefficients, and standard deviations of the reference (CALIOP) and field (modeled) SCFs are summarized in Fig. 8 as a Taylor diagram (Taylor 2001). It is apparent from Fig. 8 that out of the QMC-sampled simulations, CALIOP-169 and CALIOP-172 bear the closest resemblance in terms of their global distributions of SCF. Both simulations share similar R values at the two coldest isotherms. From Table 2, the values of epsi, the most influential parameter on SCF variance according to the GLM sensitivity analysis, for the two simulations are also relatively similar in magnitude, showing the importance of the effect of epsi on global SCF distributions. Note that Fig. 8 shows pattern RMSEs, which have the means of the field SCFs and reference SCFs removed. The correlation coefficients show the difficulty in obtaining spatial correlations with the observations with a single value of epsi used for the entire globe. For this reason, correlation coefficients were not a part of the selection criterion used in this study.

In contrast to CALIOP-169, CALIOP-7 and CALIOP-172, the worst-scoring simulation, CALIOP-50, consistently exhibits roughly the same pattern at all three isotherms (Fig. 7). CALIOP-50 has a tendency to overestimate SCF in the extratropics more than it does in the tropics and subtropics. It has some of the lowest pattern RMSEs among all the simulations, as evidenced by Fig. 8. In reference to Table 2, the near-minimally slow WBF time scale of the simulation is likely too slow for simulating SCF observations at the −30°C isotherm, while it is not slow enough at the −10° and −20°C isotherms.

A natural question to ask is how exactly epsi influences global distributions of SCF, knowing that it exerts the largest influence on SCF variance. In other words, it is interesting to determine which regions require shorter or longer WBF time scales to better reproduce observations of SCF. To quantify these effects, it is useful to utilize the SCF scores that quantify the ability of the simulation to reproduce CALIOP observations and to visualize the effect of the range of epsi in the form of box-and-whisker plots for each 20°-latitude-wide band and isotherm (Fig. 9). From the box-and-whisker plots, which categorize SCF scores by their corresponding epsi values into 16 equal groups, it is clear that no single epsi value performs equally well at all latitudes at reproducing CALIOP observations. The ability of espi to accurately reproduce CALIOP observations depends on its ability to change from region to region and from isotherm to isotherm. This finding is in agreement with the difference plots of the global distributions in SCFs shown in Fig. 7 that show the large spatial spread in SCF. As demonstrated by Fig. 9, and in agreement with Fig. 7, very slow WBF time scales (retarded between two and six orders of magnitude) are able to better reproduce CALIOP observations of SCF (i.e., have lower SCF scores) at the high latitudes at the −10°C isotherm. This is because the high-latitude regions are not affected by strong mixing processes and therefore have more subgrid-scale variability. In the tropics, however, a WBF time scale closer to that of the default model is better able to reproduce CALIOP observations of SCF at all three isotherms, as expected from the bottom two panels of Fig. 7 and consistent with Komurcu et al. (2014). The fact that the default value of the WBF process time scale, or values close to it, reproduces CALIOP observations of SCF well in the tropics can be explained by the vigorous mixing processes that make the faster WBF process time scale a good assumption in this particular region. WBF process time scales retarded by only one to two orders of magnitude relative to the default time scale in the model are better able to reproduce CALIOP observations of SCF at the −30°C isotherm, essentially at all latitudes, since this isotherm is close to the homogeneous freezing temperature, where spontaneous freezing of any liquid occurs. The coldest isotherm is therefore not as sensitive to the WBF process time scale. Like the −10°C isotherm, the −20°C isotherm requires much slower WBF processes in order to better reproduce CALIOP observations of SCF over the high latitudes of the Southern Hemisphere. Outside this latitude band, the −20°C isotherm, like the −30°C isotherm tends to better reproduce CALIOP observations of SCF when epsi is between −1 and −2. These findings suggest overall that, with the current modification to the detrainment scheme, retarding the WBF process by up to two orders of magnitude is appropriate for regions outside the tropics and extratropics in CAM5, where SCFs are highly underestimated compared to CALIOP observations. In the tropics, the default WBF process time scale is able to provide a decent match for the observations, likely because of the mixing processes present in this region. In the high latitudes, slowing the WBF process time scale by two to six orders of magnitude is more beneficial for reproducing CALIOP observations of SCF. Hence, subgrid-scale variability of cloud water at various latitudes must be taken into account. Furthermore, the pattern of SCFs in CAM5 cannot be modeled accurately on the global scale with a single epsi value for the entire globe, given the spatial variability in mixed-phase cloud partitioning.

4. Summary and conclusions

Lack of understanding and observations of cloud microphysical processes and limitations in computational resources necessitate parameterizations of cloud microphysical processes in atmospheric GCMs. These parameterizations often include arbitrary and unphysical tuning parameters that yield physically unrealistic results. Until tuning parameters can be completely eliminated from these models and replaced by purely prognostic schemes, the QMC/GLM methodology applied in the current study can be used to narrow the range of uncertainties in various microphysical parameters by providing insight into the physical explanations for shortcomings associated with parameterizations. The QMC/GLM methodology can also be used to gauge which physical processes have the largest influence on the process of interest. This information can be used for future improvements in the parameterizations of the most important processes identified by the sensitivity

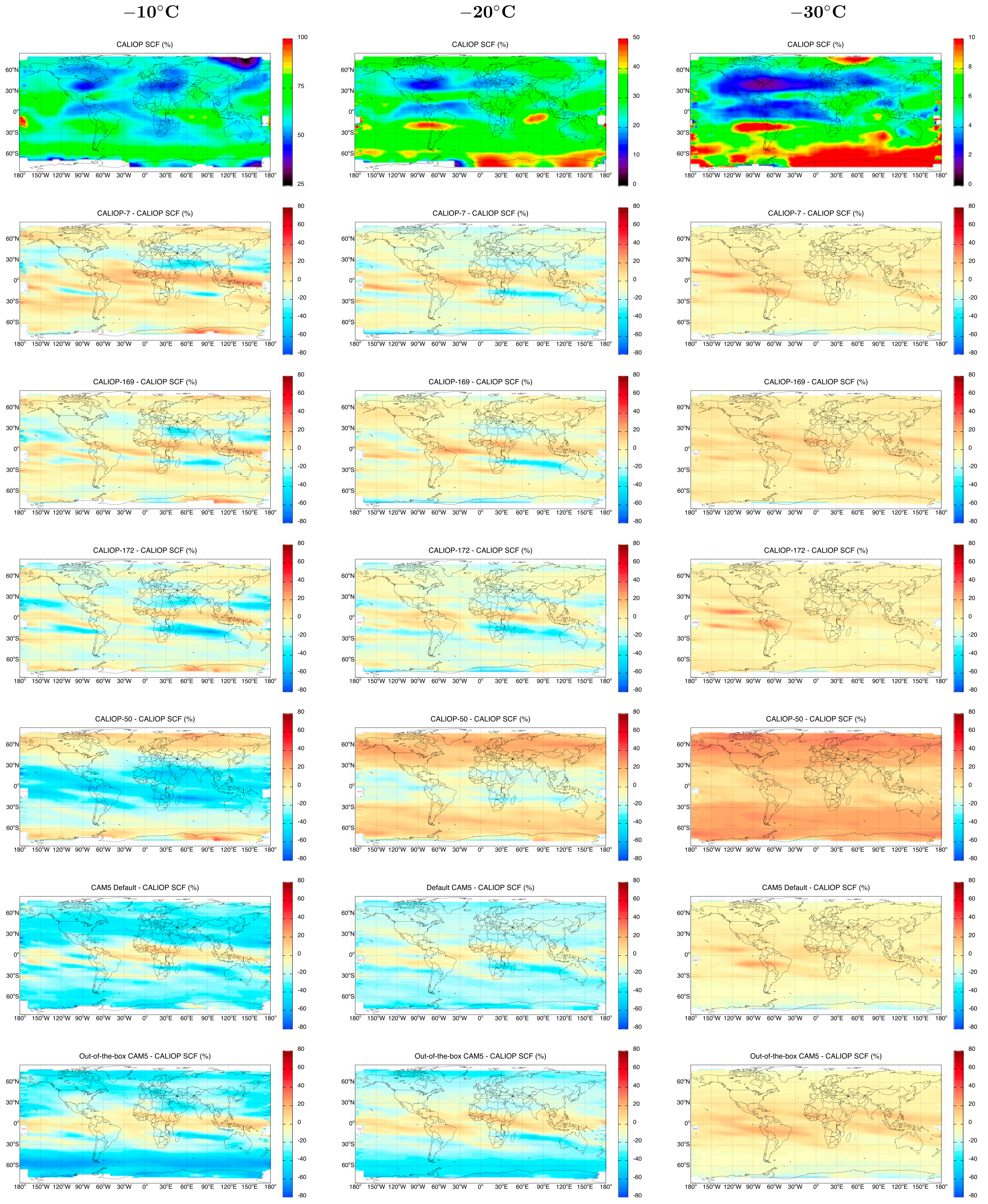

FIG. 7. Global distributions of (top) SCFs as observed by CALIOP, and their differences with (second row) CALIOP-7, (third row) CALIOP-169, (fourth row) CALIOP-172, (fifth row) CALIOP-50, (sixth row) default CAM5.1, and (bottom row) out-of-the-box CAM5.1 at the (left) −10°, (center) −20°, and (right) −30°C isotherms. CALIOP observations of SCF were calculated at a resolution of ~2.5° latitude by 2.5° longitude, limited by the NCEP–DOE Reanalysis-2 data. All CAM5.1-modeled simulations were computed at a resolution of ~4° latitude by 5° longitude. The interannual variability calculated as the standard deviation in the global, annual-mean observed SCFs are less than 1% at all three isotherms.

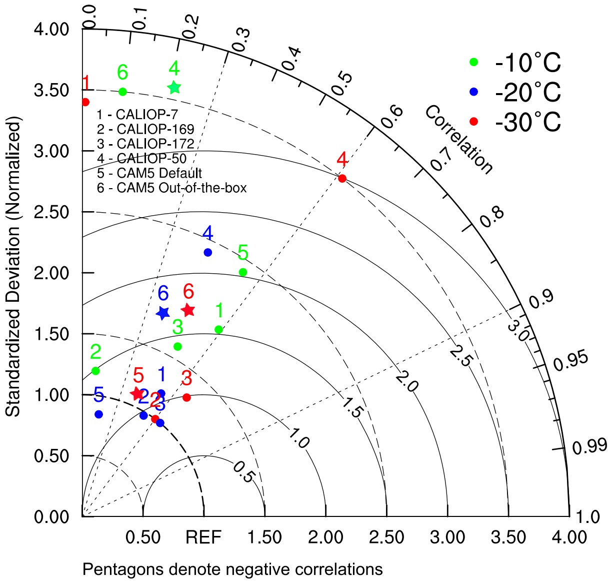

FIG. 8. Normalized Taylor diagram displaying the pattern RMSEs, correlation coefficients, and standard deviations of the reference (CALIOP observed) and field (CAM5.1 modeled) SCFs. Note that the pattern RMSEs and standard deviations have been normalized by the standard deviation of the reference field in this diagram. Note also that means of the field observations and reference observations have been subtracted in the pattern RMSEs as defined in Taylor (2001).

analysis. In this study, 256 combinations of six cloud microphysical parameters related to the partitioning between liquid and ice in mixed-phase clouds were selected by adopting a QMC sampling approach. All 256 simulations were run with a change to the convective detrainment scheme to reflect observational evidence that SCFs are underestimated by the CAM5.1. The Meyers et al. (1992) ice nucleation scheme was also replaced by the updated DeMott et al. (2015) scheme in all of the 256 simulations. The purpose of the QMC/GLM methodology was to achieve two main goals.

The first goal involved conducting sensitivity analyses on the simulations by applying a GLM to the simulations that assumes a polynomial relationship, including individual and two-way interactions effects of the six parameters. In most cases, the polynomial assumption was reasonable, as indicated by the R^2 value, which showed that the GLM could explain a large amount of the variance in CAM5.1-modeled SCFs. The GLM revealed that the WBF time scale for the growth of ice crystals at the expense of liquid droplets in mixed-phase clouds (epsi) single-handedly accounts for the vast majority of the variance in SCFs in various 20°-latitude-wide bands and at the −10°, −20°, and −30°C isotherms. Its interaction with the WBF time scale for the growth of snowflakes at the expense of liquid droplets in mixed-phase clouds (epss) was also found to play an important but secondary role in influencing SCF variance. The influence of the fraction of dust aerosols active as IN (fin) by itself and its interaction with epsi on SCF variance was evident mostly in latitude bands covering large desert regions (10°–50°N) and over the Southern Ocean (58°–90°S). Although the GLM sensitivity analysis applied in this study is limited to two-way interaction effects, it appears that a common sequence of events is that, in regions with high concentrations of dust, ice nucleation on dust particles and the subsequent formation of ice crystals is likely highly influenced by the WBF time scale for ice. The individual influence of ice crystal fall speed (ai) only appears to contribute noticeably to SCF variance at the two colder isotherms examined in this study, where ice is expected to be more prevalent.

The second objective of the study was to select 3 out of the 256 QMC-sampled simulations that best reproduce CALIOP observations of SCF based on a defined score (the CS score), meant to select the simulation that most closely reproduces observations on the whole, as well as other selection criteria that opted for simulations with parameter values that together span a wide range. All simulations, including the simulation deemed the worst match to CALIOP observations, were better at reproducing CALIOP observations than the out-of-the-box CAM5.1 model, which consistently severely underestimated SCFs at almost all latitudes and isotherms. In the two control simulations, the −30°C isotherm performed, by far, the best out of the three isotherms. This can be explained by the fact that the isotherm, even though far from regions of strong mixing, is close to the homogeneous freezing temperature, where virtually all liquid freezes, and the WBF process time scale is therefore not as relevant. In regions with vigorous mixing processes, such as the tropics, the default WBF process time scale reproduced CALIOP observations of SCF quite well, since this region is well mixed and therefore not sensitive to subgrid-scale variability. In the extratropics and high latitudes, where efficient mixing processes like those over the tropics do not exist, retarding the WBF process time scale by one to two orders of magnitude in the extratropics and between two and six orders of magnitude in the high latitudes results in better agreement in SCFs with the observations. CALIOP-169 and CALIOP-172 have similar epsi values and produced similar patterns in SCFs at the three isotherms. The simulation with the highest CS score [i.e., the simulation deemed the worst match to CALIOP observations (CALIOP-50)] consistently overestimated SCFs at higher latitudes and underestimated SCFs at lower latitudes.

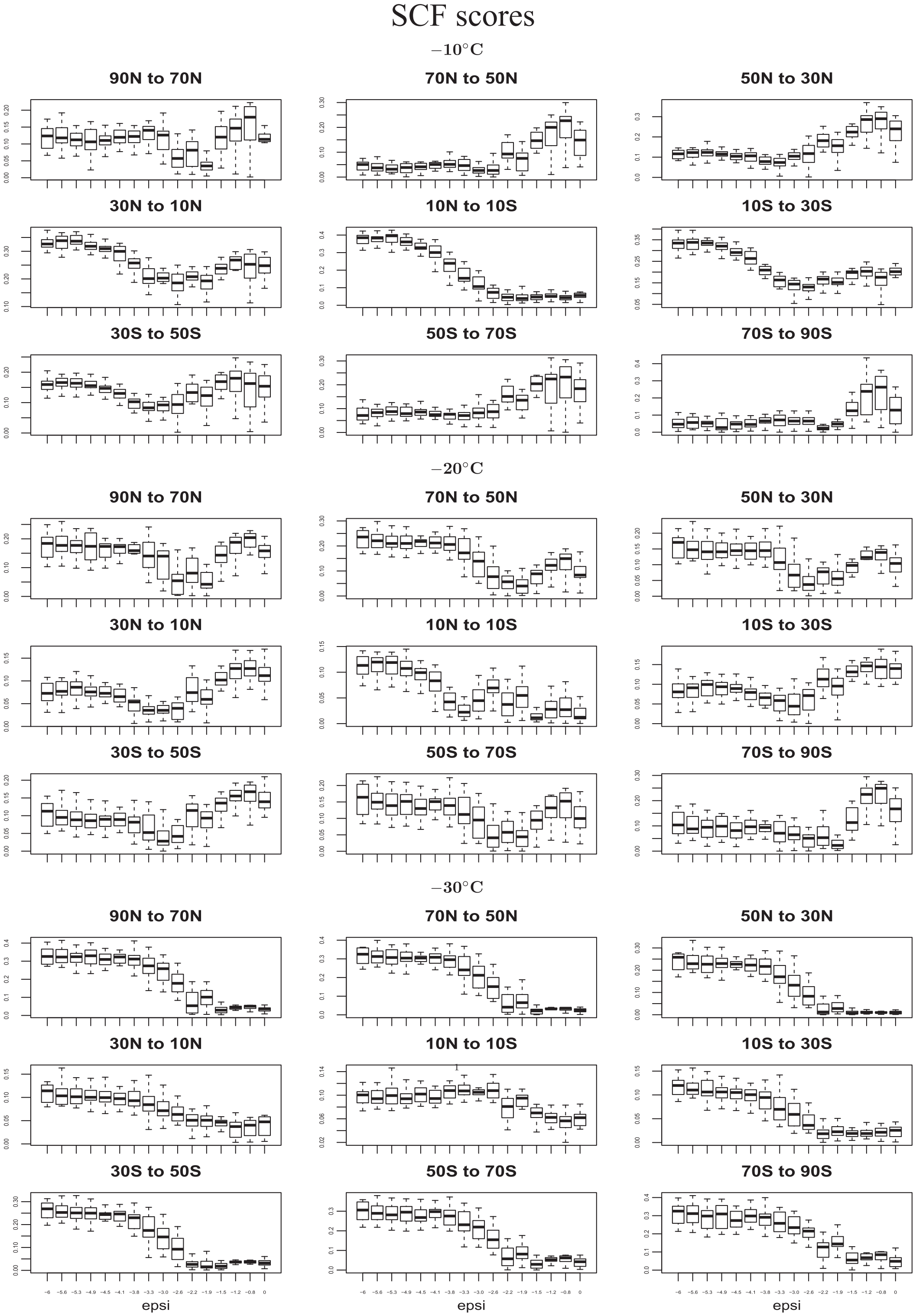

FIG. 9. Box-and-whisker plots of the SCF scores of the 256 QMC-sampled simulations, grouped into 16 equally divided bins based on their epsi values such that each bin contains 16 simulations. Plots for each of the nine latitude bands are displayed at the (top) −10°, (middle) −20°, and (bottom) −30°C isotherms. The boxes display the median, lower, and upper quartiles and minimum and maximum values within each bin. Outliers are not shown.

In conclusion, this study demonstrates the critical importance of the WBF time scales involving ice and snow for influencing SCFs on the global scale. In nature, mixed-phase clouds are rarely composed of homogeneous mixtures of liquid and ice, but rather, have a tendency to exist as inhomogeneous pockets of ice crystals and supercooled liquid droplets that are orders of magnitude smaller in volume than grid boxes typical of atmospheric GCMs. The results of this study show that failing to account for this effect could potentially explain the vast majority of the severe underestimate in SCFs seen especially in the extratropics in most atmospheric GCMs. Given the importance of cloud thermodynamic phase on the radiative properties of clouds, improvements to the parameterizations in the WBF process could thus potentially improve climate projections.

Acknowledgments. This work was supported by NASA Headquarters under the NASA Earth and Space Science Fellowship Program, Grant NNX14AL07H. The authors would also like to acknowledge high-performance computing support from Yellowstone (ark:/85065/d7wd3xhc) provided by NCAR's Computational and Information Systems Laboratory, sponsored by the National Science Foundation under Grant AGS-1352417. NCEP–DOE Reanalysis-2 data were provided by the NOAA/OAR/ESRL PSD, Boulder, Colorado, from their website (http://www.esrl.noaa.gov/psd/).

APPENDIX

Equations

The primary driving equations in which the six cloud microphysical tuning parameters appear are provided in the following sections.

a. *Wegener–Bergeron–Findeisen process time scale for ice*

The local in-cloud deposition rate of water vapor onto cloud ice A is given by

$$A = \frac{q_v^* - q_{vi}^*}{\Gamma_p \tau_i}, \qquad \text{(A1)}$$

where q_v^* is the in-cloud water vapor mixing ratio, q_{vi}^* is the in-cloud water vapor mixing ratio at ice saturation, and Γ_p is the psychrometric correction to account for the release of latent heat given by

$$\Gamma_p = 1 + \frac{L_s}{c_p}\frac{dq_{vi}}{dT}, \qquad \text{(A2)}$$

where L_s is the latent heat of sublimation, c_p is the specific heat capacity at constant pressure, and dq_{vi}/dT is the change of ice saturation vapor pressure with temperature. The supersaturation relaxation time scale for ice deposition (i.e., the inverse of epsi) is given by

$$\tau_i = (2\pi N_{0i}\rho_a D_v \lambda_i^{-2})^{-1}, \qquad \text{(A3)}$$

where ρ_a is the density of air, D_v is the diffusivity of water vapor in air, and N_{0i} and λ_i are the intercept and slope of the ice size distribution, respectively, represented by the gamma function:

$$\phi(D) = N_{0i} D^{\mu} \exp^{-\lambda_i D}, \qquad \text{(A4)}$$

where D is the diameter, and μ is the spectra shape parameter, which is set to zero for cloud ice. If $A > Q$, where Q is the gridbox-averaged difference in the rate of condensation and evaporation of cloud water and ice, then the growth of ice through the WBF process occurs at the expense of the surrounding cloud liquid water. The total grid-scale condensation growth rate of ice is given by

$$\left(\frac{\partial q_i}{\partial t}\right)_{\text{cond}} = \min\left(F_{\text{cld}}A, F_{\text{cld}}Q + \frac{q_c}{\Delta t}\right), \qquad \text{(A5)}$$

where q_i is the mixing ratio of cloud ice, F_{cld} is the cloud fraction, and Δt is the model time step. The order of magnitude estimate of the retardation factor of the WBF time scale is derived as follows. The volume of a typical GCM grid box is $O(1)\,\text{km} \times O(100)\,\text{km} \times O(100)\,\text{km} = O(10^{13})\,\text{m}^3$ (see Fig. 2). In the most extreme case, pockets purely composed or liquid droplets or ice crystals can extend down to $O(10)\,\text{m}$ in the horizontal (Chylek and Borel 2004). When subgrid-scale variability is neglected, the mixing zone where liquid droplets and ice crystals interact via the WBF process spans the entire grid box. When subgrid-scale variability is taken into account, the mixing zones decrease in volume. In the most extreme case found in the Arctic where the pockets extend $\sim O(100)\,\text{m}$ horizontally, there would be alternating pockets of liquid droplets and ice crystals, separated by mixing zones that are less than $O(100)\,\text{m}$ wide in the horizontal. Taking the width of the mixing zone to be $O(1)\,\text{m}$, this implies that there would be 10^3 (10) alternating pockets of liquid droplets and ice crystals in the horizontal (vertical) directions. Thus, the total mixing zone volume would be $O(10^3)\,\text{m} \times O(10^3)\,\text{m} \times O(10)\,\text{m} = O(10^7)\,\text{m}^3$. This volume is six orders of magnitude smaller than that of the mixing zone if homogeneous mixtures of liquid droplets of ice are assumed. The difference is reflected in the WBF time scale.

b. Wegener–Bergeron–Findeisen process time scale for snow

All equations are identical to those in the previous section except for Eq. (A3), which is instead replaced by τ_s, which is the inverse of epss and is defined as

$$\tau_s = \left\{ 2\pi N_{0s} \rho_a D_v \left[f_{v_1} \lambda_s^{-2} + f_{v_2} \sqrt{\frac{\rho_{as}\rho_a}{\mu_a}} \mathrm{Sc}^{1/3} \Gamma\left(\frac{5}{2} + \frac{b_s}{2}\right) \lambda_s^{5/2+b_s/2} \right] \right\}^{-1}, \tag{A6}$$

where N_{0s} and λ_s are the intercept and slope of the snow size distribution, respectively, f_{v_1} and f_{v_2} are ventilation factors for snow fixed at 0.86 and 0.28, respectively, μ_a is the viscosity of air, Sc is the Schmidt number, b_s is an empirical coefficient fixed at 0.41 for snow and is related to the terminal fall speed for an individual particle V by $V = a_s D_s^b$, where a is another empirical parameter fixed at $11.72\,\mathrm{m}^{1-b_s}\,\mathrm{s}^{-1}$ for snow and D is the particle diameter, and ρ_{as} is the air density correction factor for snow given by $\rho_{as} = (\rho_a/\rho_{a0})^{0.54}$, where ρ_{a0} is the air density at 850 hPa and 0°C.

c. Ice crystal fall speed

The parameter related to the ice crystal fall speed, ai, relates the terminal fall speed for an individual ice particle through the same relation described in section b above, except that b is instead fixed at 1 (i.e., $V = a_i D^{b_i}$, where $b_i = 1$). We use a (or a_i as written in the previous equation) in the mass- and number-weighted terminal fall speeds for all cloud and precipitation species (V_q and V_N, respectively), given by

$$V_N = \frac{\int_0^\infty (\rho_a/\rho_{a0})^{0.54} a D^b \phi(D)\,dD}{\int_0^\infty \phi(D)\,dD} = \frac{(\rho_a/\rho_{a0})^{0.54} a \Gamma(1+b+\mu)}{\lambda^b \Gamma(\mu+1)} \quad \text{and} \tag{A7}$$

$$V_q = \frac{\int_0^\infty (\pi\rho/6)(\rho_a/\rho_{a0})^{0.54} a D^{b+3} \phi(D)\,dD}{\int_0^\infty (\pi\rho/6) D^3 \phi(D)\,dD} = \frac{(\rho_a/\rho_{a0})^{0.54} a \Gamma(4+b+\mu)}{\lambda^b \Gamma(\mu+4)}, \tag{A8}$$

where ρ_{a0} is the reference air density at standard temperature and pressure.

d. Fraction of ice nuclei active in ice nucleation

The concentration of active IN in the original Meyers et al. (1992) scheme is replaced by

$$n_{\mathrm{INP},T_k} = \mathrm{fin} F n_{a>0.5\mu\mathrm{m}}^{\alpha(273.16-T_k)+\beta} e^{\gamma(273.16-T_k)+\delta}, \tag{A13}$$

where fin is the tuning factor used in this study to control the fraction of IN active in ice nucleation; F is the calibration factor, recommended to be set to 3 for atmospheric data; the empirical constants $\alpha = -0.074$, $\beta = 3.8$, $\gamma = 0.414$ and $\delta = -9.671$; T_k is the cloud temperature (K); n_{INP,T_k} is the ice nucleating particle number concentration (L^{-1}) at cloud temperature T_k; and $n_{a>0.5\mu\mathrm{m}}$ is the number concentration of aerosol particles with diameters larger than 0.5 μm (cm^{-3}).

e. Fraction of aerosols scavenged in stratiform and convective clouds

The parameters sol_facti and sol_factic are solubility factors that can be interpreted as the product of the fraction of aerosols in cloud droplets and an additional tuning factor. The total in-cloud scavenging for stratiform clouds $S_{\mathrm{strat,tot}}$ is given by

$$S_{\mathrm{strat,tot}} = \frac{1}{\Delta t}\mathrm{sol\_facti} f_p C(1-f_i) + \frac{1}{\Delta t}\mathrm{sol\_factii} f_p C(1-f_i), \tag{A14}$$

where f_p is the fraction of cloud water converted to precipitation, sol_factii is the fraction of aerosols scavenged in stratiform ice clouds, C is the tracer mixing ratio, f_i is the fraction of cloud condensate in the ice phase, and Δt is the model time step. The total in-cloud scavenging for convective clouds is

$$S_{\mathrm{conv,tot}} = \frac{1}{\Delta t}\mathrm{sol\_factic} f_t f_p C(1-f_i) + \frac{1}{\Delta t}\mathrm{sol\_factiic} f_p C(1-f_i), \tag{A15}$$

where f_t is the total cloud fraction and sol_factiic is the fraction of aerosols scavenged in convective ice clouds.

REFERENCES

Atkinson, J. D., and Coauthors, 2013: The importance of feldspar for ice nucleation by mineral dust in mixed-phase clouds. *Nature*, **498**, 355–358, doi:10.1038/nature12278.

Bigg, E. K., 1953: The supercooling of water. *Proc. Phys. Soc.*, **66B**, 688–694, doi:10.1088/0370-1301/66/8/309.

Boucher, O., and Coauthors, 2013: Clouds and aerosols. *Climate Change 2013: The Physical Science Basis*, T. F. Stocker et al., Eds., Cambridge University Press, 571–658. [Available online at http://www.ipcc.ch/pdf/assessment-report/ar5/wg1/WG1AR5_Chapter07_FINAL.pdf.]

Caflisch, R. E., 1998: Monte Carlo and quasi–Monte Carlo methods. *Acta Numer.*, **7**, 1–49, doi:10.1017/S0962492900002804.

Cesana, G., and H. Chepfer, 2013: Evaluation of the cloud thermodynamic phase in a climate model using CALIPSO-GOCCP. *J. Geophys. Res. Atmos.*, **118**, 7922–7937, doi:10.1002/jgrd.50376.

——, D. E. Waliser, X. Jiang, and J.-L. F. Li, 2015: Multimodel evaluation of cloud phase transition using satellite and reanalysis data. *J. Geophys. Res. Atmos.*, **120**, 7871–7892, doi:10.1002/2014JD022932.

Chepfer, H., G. Broginez, P. Goloub, F. M. Bréon, and P. H. Flamant, 1999: Observations of horizontally oriented ice crystals in cirrus clouds with POLDER-1/ADEOS-1. *J. Quant. Spectrosc. Radiat. Transfer*, **63**, 521–543, doi:10.1016/S0022-4073(99)00036-9.

Choi, Y.-S., R. S. Lindzen, C.-H. Ho, and J. Kim, 2010: Space observations of cold-cloud phase change. *Proc. Natl. Acad. Sci. USA*, **107**, 11 211–11 216, doi:10.1073/pnas.1006241107.

——, C.-H. Ho, C.-E. Park, T. Storelvmo, and I. Tan, 2014: Influence of cloud phase composition on climate feedbacks. *J. Geophys. Res. Atmos.*, **119**, 3687–3700, doi:10.1002/2013JD020582.

Chylek, P., and C. Borel, 2004: Mixed phase cloud water/ice structure from high spatial resolution satellite data. *Geophys. Res. Lett.*, **31**, L14104, doi:10.1029/2004GL020428.

Conen, F., S. Rodríguez, C. Hüglin, S. Henne, E. Herrmann, N. Bukowiecki, and C. Alewell, 2015: Atmospheric ice nuclei at the high-altitude observatory, Jungfraujoch, Switzerland. *Tellus*, **67B**, 25014, doi:10.3402/tellusb.v67.25014.

Cotton, W. R., G. J. Tripoli, R. M. Rauber, and E. A. Mulvihill, 1986: Numerical simulation of the effects of varying ice crystal nucleation rates and aggregation processes on orographic snowfall. *J. Climate Appl. Meteor.*, **25**, 1658–1680, doi:10.1175/1520-0450(1986)025<1658:NSOTEO>2.0.CO;2.

DeMott, P. J., and Coauthors, 2015: Integrating laboratory and field data to quantify the immersion freezing ice nucleation activity of mineral dust particles. *Atmos. Chem. Phys.*, **15**, 393–409, doi:10.5194/acp-15-393-2015.

Eidhammer, T., H. Morrison, A. Bansemer, A. Gettelman, and A. J. Heymsfield, 2014: Comparison of ice cloud properties simulated by the Community Atmosphere Model (CAM5) with in-situ observations. *Atmos. Chem. Phys.*, **14**, 10 103–10 118, doi:10.5194/acp-14-10103-2014.

Fan, J., S. Ghan, M. Ovchinnikov, X. Liu, P. J. Rasch, and A. Korolev, 2011: Representation of Arctic mixed-phase clouds and the Wegener–Bergeron–Findeisen process in climate models: Perspectives from a cloud-resolving study. *J. Geophys. Res.*, **116**, D00T07, doi:10.1029/2010JD015375.

Field, P. R., R. J. Hogan, P. R. A. Brown, A. J. Illingworth, T. W. Choularton, P. H. Kaye, E. Hirst, and R. Greenaway, 2004: Simultaneous radar and aircraft observations of mixed-phase cloud at the 100 m scale. *Quart. J. Roy. Meteor. Soc.*, **130**, 1877–1904, doi:10.1256/qj.03.102.

Ghan, S. J., L. R. Leung, and R. C. Easter, 1997: Prediction of cloud droplet number in a general circulation model. *J. Geophys. Res.*, **102**, 21 777–21 794, doi:10.1029/97JD01810.

Hobbs, P. V., and A. L. Rangno, 1998: Microstructures of low and middle-level clouds over the Beaufort Sea. *Quart. J. Roy. Meteor. Soc.*, **124**, 2035–2071, doi:10.1002/qj.49712455012.

——, ——, L. Arthur, M. Shupe, and T. Uttal, 2001: Airborne studies of cloud structures over the Arctic Ocean and comparisons with retrievals from ship-based remote sensing measurements. *J. Geophys. Res.*, **106**, 15 029–15 044, doi:10.1029/2000JD900323.

Hu, Y., and Coauthors, 2009: *CALIPSO*/CALIOP cloud phase discrimination algorithm. *J. Atmos. Oceanic Technol.*, **26**, 2293–2309, doi:10.1175/2009JTECHA1280.1.

Kanamitsu, M., W. Ebisuzaki, W. Woollen, S.-K. Yang, J. J. Hnilo, M. Fiorino, and G. L. Potter, 2002: NCEP–DOE AMIP-II Reanalysis (R-2). *Bull. Amer. Meteor. Soc.*, **83**, 1631–1643, doi:10.1175/BAMS-83-11-1631.

Koffi, B., and Coauthors, 2012: Application of the CALIOP layer product to evaluate the vertical distribution of aerosols estimated by global models: AeroCom phase I results. *J. Geophys. Res.*, **117**, D10201, doi:10.1029/2011JD016858.

Komurcu, M., and Coauthors, 2014: Intercomparison of the cloud water phase among global climate models. *J. Geophys. Res. Atmos.*, **119**, 3372–3400, doi:10.1002/2013JD021119.

Korolev, A. V., G. A. Isaac, S. Cober, J. W. Strapp, and J. Hallett, 2003: Microphysical characterization of mixed-phase clouds. *Quart. J. Roy. Meteor. Soc.*, **129**, 39–65, doi:10.1256/qj.01.204.

Li, Z.-X., and H. LeTreut, 1992: Cloud-radiation feedbacks in a general circulation model and their dependence on cloud modelling assumptions. *Climate Dyn.*, **7**, 133–139, doi:10.1007/BF00211155.

Liu, X., and Coauthors, 2012: Toward a minimal representation of aersols in climate models: Description and evaluation in the Community Atmosphere Model CAM5. *Geosci. Model Dev.*, **5**, 709–739, doi:10.5194/gmd-5-709-2012.

Liu, Z., and Coauthors, 2009: The *CALIPSO* lidar cloud and aerosol discrimination: Version 2 algorithm and initial assessment of performance. *J. Atmos. Oceanic Technol.*, **26**, 1198–1213, doi:10.1175/2009JTECHA1229.1.

McCoy, D. T., D. L. Hartmann, and D. P. Grosvenor, 2014: Observed Southern Ocean cloud properties and shortwave reflection. Part I: Calculation of SW flux from observed cloud properties. *J. Climate*, **27**, 8836–8857, doi:10.1175/JCLI-D-14-00287.1.

McFarlane, N., 2011: Parameterizations: Representing key processes in climate models without resolving them. *Wiley Interdiscip. Rev.: Climate Change*, **2**, 482–497, doi:10.1002/wcc.122.

Meyers, M. P., P. J. DeMott, and W. R. Cotton, 1992: New primary ice-nucleation parameterizations in an explicit cloud model. *J. Appl. Meteor.*, **31**, 708–721, doi:10.1175/1520-0450(1992)031<0708:NPINPI>2.0.CO;2.

Mioche, G., O. Jourdan, M. Ceccaldi, and J. Delanoë, 2015: Variability of mixed-phase clouds in the Arctic with a focus on the Svalbard region: A study based on spaceborne active remote sensing. *Atmos. Chem. Phys.*, **15**, 2445–2461, doi:10.5194/acp-15-2445-2015.

Mitchell, J. F. B., C. A. Senior, and W. J. Ingram, 1989: CO_2 and climate: A missing feedback? *Nature*, **341**, 132–134, doi:10.1038/341132a0.

Morrison, H., and A. Gettelman, 2008: A new two-moment bulk stratiform cloud microphysics scheme in the Community Atmosphere Model, version 3 (CAM3). Part I: Description and numerical tests. *J. Climate*, **21**, 3642–3659, doi:10.1175/2008JCLI2105.1.

Naumann, A. K., A. Seifert, and J.-P. Mellado, 2013: A refined statistical cloud closure using double-Gaussian probability density functions. *Geosci. Model Dev.*, **6**, 1641–1657, doi:10.5194/gmd-6-1641-2013.

Neale, R. B., and Coauthors, 2010: Description of the NCAR Community Atmosphere Model (CAM5.0). NCAR Tech. Note NCAR/TN-486+STR, 274 pp. [Available online at http://www.cesm.ucar.edu/models/cesm1.0/cam/docs/description/cam5_desc.pdf.]

Noel, V., and H. Chepfer, 2010: A global view of horizontally oriented crystals in ice clouds from *Cloud–Aerosol Lidar And Infrared Pathfinder Satellite Observation* (*CALIPSO*). *J. Geophys. Res.*, **115**, D00H23, doi:10.1029/2009JD012365.

Omar, A. H., and Coauthors, 2009: The *CALIPSO* automated aerosol classification and lidar ratio selection algorithm. *J. Atmos. Oceanic Technol.*, **26**, 1994–2014, doi:10.1175/2009JTECHA1231.1.

Pincus, R., and S. A. Klein, 2000: Unresolved spatial variability and microphysical process rates in large-scale models. *J. Geophys. Res.*, **105**, 27 059–27 065, doi:10.1029/2000JD900504.

Pinto, J. O., 1998: Autumnal mixed-phase cloudy boundary layers in the Arctic. *J. Atmos. Sci.*, **55**, 2016–2038, doi:10.1175/1520-0469(1998)055<2016:AMPCBL>2.0.CO;2.

Rotstayn, L. D., 2000: On the ''tuning'' of autoconversion parameterizations in climate models. *J. Geophys. Res.*, **105**, 15 495–15 507, doi:10.1029/2000JD900129.

Salzmann, M., Y. Ming, J.-C. Golaz, P. A. Ginoux, H. Morrison, A. Gettelman, M. Krämer, and L. J. Donner, 2010: Two-moment bulk stratiform cloud microphysics in the GFDL AM3 GCM: Description, evaluation, and sensitivity tests. *Atmos. Chem. Phys.*, **10**, 8037–8064, doi:10.5194/acp-10-8037-2010.

Shupe, M. D., 2011: Clouds at Arctic atmospheric observatories. Part II: Thermodynamic phase characteristics. *J. Appl. Meteor. Climatol.*, **50**, 645–661, doi:10.1175/2010JAMC2468.1.

Song, X., and G. J. Zhang, 2011: Microphysics parameterization for convective clouds in a global climate model: Description and single-column model tests. *J. Geophys. Res.*, **116**, D02201, doi:10.1029/2010JD014833.

Storelvmo, T., J. E. Kristjánsson, U. Lohmann, T. Iversen, A. Kirkevåg, and Ø. Seland, 2008: Modeling of the Wegener–Bergeron–Findeisen process—Implications for aerosol indirect effects. *Environ. Res. Lett.*, **3**, 045001, doi:10.1088/1748-9326/3/4/045001.

Tan, I., T. Storelvmo, and Y.-S. Choi, 2014: Spaceborne lidar observations of the ice-nucleating potential of dust, polluted dust, and smoke aerosols in mixed-phase clouds. *J. Geophys. Res. Atmos.*, **119**, 6653–6665, doi:10.1002/2013JD021333.

Taylor, K. E., 2001: Summarizing multiple aspects of model performance in a single diagram. *J. Geophys. Res.*, **106**, 7183–7192, doi:10.1029/2000JD900719.

Tompkins, A. M., 2002: A prognostic parameterization for the subgrid-scale variability of water vapor and clouds in large-scale models and its use to diagnose cloud cover. *J. Atmos. Sci.*, **59**, 1917–1942, doi:10.1175/1520-0469(2002)059<1917:APPFTS>2.0.CO;2.

Tsushima, Y., and Coauthors, 2006: Importance of the mixed-phase cloud distribution in the control climate for assessing the response of clouds to carbon dioxide increase: A multi-model study. *Climate Dyn.*, **27**, 113–126, doi:10.1007/s00382-006-0127-7.

Young, K. C., 1974: The role of contact nucleation in ice phase initiation of clouds. *J. Atmos. Sci.*, **31**, 768–776, doi:10.1175/1520-0469(1974)031<0768:TROCNI>2.0.CO;2.

Zelinka, M. D., S. A. Klein, and D. L. Hartmann, 2012: Computing and partitioning cloud feedbacks using cloud property histograms. Part II: Attribution to changes in cloud amount, altitude, and optical depth. *J. Climate*, **25**, 3736–3754, doi:10.1175/JCLI-D-11-00249.1.

Zhao, C., and Coauthors, 2013: A sensitivity study of radiative fluxes at the top of atmosphere to cloud-microphysics and aerosol parameters in the community atmosphere model CAM5. *Atmos. Chem. Phys.*, **13**, 10 969–10 987, doi:10.5194/acp-13-10969-2013.

Zhou, C., P. Yang, A. E. Dessler, and F. Liang, 2013: Statistical properties of horizontally oriented plates in optically thick clouds from satellite observations. *Geosci. Remote Sens. Lett.*, **10**, 986–990, doi:10.1109/LGRS.2012.2227451.